Mechanisms and systematics of breakup in reactions of ^{9}Be at near-barrier energies

R. Rafiei,* R. du Rietz, D. H. Luong, D. J. Hinde, M. Dasgupta, M. Evers, and A. Diaz-Torres†
Department of Nuclear Physics, Research School of Physics and Engineering, The Australian National University, Canberra, ACT 0200, Australia
(Received 2 December 2009; published 5 February 2010)

Below-barrier no-capture breakup measurements of the weakly bound ^{9}Be nucleus, incident on targets ranging in atomic number from 62 to 83, have been carried out using a large-area high-resolution back-angle detector array. It is shown that the three-body reconstructed reaction Q-value and relative energy of the breakup fragments together reveal the full dynamics of the breakup mechanism, identifying all physical processes that lead to the breakup of the projectile-like nucleus. Contrasting with the simple expectation of direct breakup into the most energetically favored clusters, the data show that breakup following n-transfer dominates the total breakup yield. Breakup from long-lived states in the projectile-like nucleus, which on the reaction time scale may be considered stable, has been isolated from the prompt breakup yield. It has been shown that the prompt breakup probability essentially depends on the surface separation of the interacting nuclei. The measured prompt breakup probability functions for each target have been used together with a classical trajectory model to predict the above-barrier suppression of complete fusion. The suppression factor, expressed as the fraction of incomplete fusion, is nearly independent of target charge.

DOI: 10.1103/PhysRevC.81.024601 PACS number(s): 25.60.Gc, 25.70.Hi, 25.70.Mn, 25.70.Pq

I. INTRODUCTION

Interactions of the most weakly bound stable nuclei, ^{6,7}Li and ^{9}Be, display a range of anomalous behaviors, all attributed to the low threshold energy for breakup into their cluster constituents [1]. Over the last decade, with the availability of secondary radioactive ion beams, understanding the role of breakup in fusion has become a major research focus [1–3]. An intensive experimental and theoretical program, made possible by precision measurements using stable weakly bound nuclei [4–21], has been pursued to understand the interplay between breakup and fusion dynamics.

Projectile breakup modifies the accepted picture for two-body fusion of strongly bound nuclei [22]. Reaction outcomes must now include (i) complete fusion (CF), often defined for experimental reasons as the sum of two-body fusion and breakup followed by full projectile charge absorption [4,12]; (ii) incomplete fusion (ICF) or breakup fusion, which originates from projectile breakup followed by absorption of one of the charged breakup fragments; and (iii) no-capture breakup (NCBU), where no breakup fragment is captured by the target. The resulting interactions between the projectile fragments and the target form a complex N-body ($N \geqslant 3$) problem. Precision CF excitation functions reported for $^{9}\mathrm{Be} + {}^{208}\mathrm{Pb}$ [4,12] and $^{6,7}\mathrm{Li} + {}^{209}\mathrm{Bi}$ [7,12] show above-barrier cross sections only 0.70 ± 0.04 of those expected for well-bound nuclei. Following CF measurements for the $^{9}\mathrm{Be} + {}^{208}\mathrm{Pb}$ reaction [4], experiments were carried out [23] to determine whether breakup processes could be responsible for the suppression of CF. Measurements were made at sub-barrier energies, where capture is negligible, and allowed the probabilities of NCBU alone to be investigated. From the singles α spectra the prompt breakup yield was determined. The probability for projectile prompt breakup was described as a function of the distance of closest approach on a classical trajectory, which is referred to here as the breakup function. Extrapolation of the breakup function to above-barrier energies showed [23] that *qualitatively* breakup can explain the measured above-barrier suppression of CF [4]. A three-dimensional classical dynamical model [24] was subsequently developed to relate above-barrier CF and ICF cross sections with below-barrier NCBU cross sections. This mapping utilizes the experimentally measured breakup function obtained from sub-barrier NCBU probabilities. It was found [24] that sub-barrier breakup probabilities could be *quantitatively* mapped to above-barrier ICF and CF cross sections and, thus, to the CF suppression.

The remaining problem is to determine the mechanisms responsible for triggering breakup. The systematics of above-barrier CF suppression factors were presented in Ref. [21] for ^{6,7}Li, ^{9}Be, and ^{10,11}B on a range of heavy targets [8,11,12,17,18]. The fraction of ICF for all projectiles incident on ^{209}Bi and ^{208}Pb targets was shown to be an exponential function of the projectile breakup threshold. This observation suggests that the suppression of CF is associated with direct breakup into the most energetically favored cluster constituents. However, theoretical predictions of the mechanism for breakup using a two-center shell model for $^{9}\mathrm{Be} + {}^{209}\mathrm{Bi}$ [25] suggest that a likely breakup channel should be via excited states in ^{8}Be, produced following the transfer of the single valence neutron to ^{209}Bi.

The measurements presented in this work were carried out with the aim of investigating reaction mechanisms leading to breakup and their links to the systematics of CF suppression. The experiment utilized ^{9}Be projectiles, incident on targets ranging in atomic number from $Z = 62$ to $Z = 83$.

*ramin.rafiei@anu.edu.au
†Present address: Department of Physics, University of Surrey, Guildford, Surrey GU2 7XH, United Kingdom.

 ©2010 The American Physical Society

Measurements were made by coincident detection of the breakup α particles [26] at sub-barrier energies, where the probability of capture of a charged breakup fragment by the target nucleus is negligible. A highly pixelated, large-solid-angle detector array made possible reconstruction of the coincident α-particle properties, providing new insights into the breakup mechanism and systematics.

Section II details the experimental setup and measurement technique used. Characterization of breakup events using the reconstructed Q-value and relative energy is demonstrated in Sec. III. Section IV identifies the physical mechanisms that lead to the breakup of the projectile-like nucleus. Determination of the breakup probability function and the systematics of breakup are presented in Sec. V and Sec. VI, respectively. Systematics of above-barrier CF suppression owing to breakup are detailed in Sec. VII.

II. EXPERIMENTAL SETUP AND ANALYSIS PROCEDURE

The experiment was carried out at the Australian National University, using ^{9}Be beams from the 14UD tandem electrostatic accelerator. The beams were incident on isotopically enriched targets at energies ranging from deep sub-barrier to the barrier energy, as reported in Table I. All targets were evaporated onto $\sim$15 μg cm^{-2} $^{\text{nat}}$C backings with the exception of ^{209}Bi and ^{196}Pt, which were self-supporting. The targets were oriented at 90° to the beam axis, with their backing, if present, facing downstream, thus minimizing the energy loss of the breakup fragments.

Breakup fragments were detected using an array of four large-area double-sided silicon-strip detectors covering 0.84π sr in the backward hemisphere. A schematic drawing of the array is shown in Fig. 1. Individual detectors were angled 45° toward the beam axis and mounted on a hub coaxial with the beam axis. The front face of each detector is divided into 16 arcs and the back face is divided into 8 sectors. The intersection of each arc and sector defines a pixel. Each 6.4 mm wide arc and each sector, spanning 6.67°, is separated from its neighbor by a 100 μm insulating partition. Each detector has a thickness of 400 μm and a front and back aluminium electrode coating of 200 nm, across which the bias voltage was applied. A 0.7 μm Mylar foil was placed in front of each detector to stop low-energy electrons. The array was shielded from beam particles scattered downstream of the target by an aluminium sheet located in the plane of the target ladder.

TABLE I. Target material, thickness (t), and laboratory beam energy ranges (inclusive) for this experiment. Measurements were made at laboratory energy intervals of 3 MeV. Center-of-mass barrier energies (V_b), calculated using the Sao Paulo potential (SPP) [27,28], are also listed.

Target	t (μg cm^{-2})	E_{beam} (MeV)	V_b (MeV)
^{209}Bi	400	28–40	38.98
^{208}PbS	80	28–40	38.52
^{196}Pt	120	25–37	37.05
^{186}W	80	25–37	35.47
^{168}Er	50	25–34	33.20
^{144}Sm	100	25–34	31.18

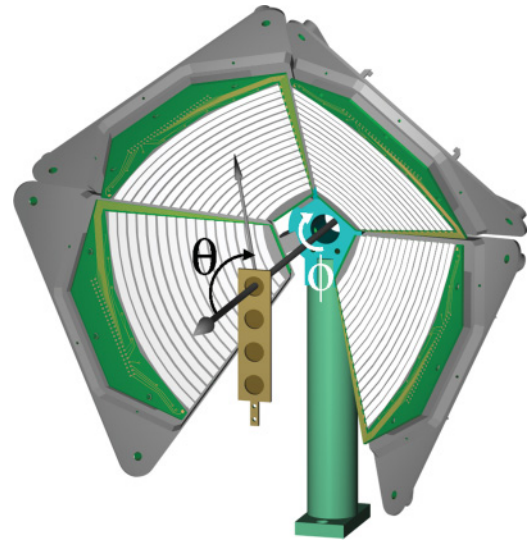

FIG. 1. (Color online) Schematic drawing of the double-sided silicon-strip detector array. The reference coordinate system used in the kinematic analysis is shown. The beam is marked by the arrow pointing through the target ladder (in the foreground) and out of the page. See text for details.

The 64 arcs and 32 sectors were individually read out using 16-channel charge-sensitive preamplifiers and 16-channel amplifier modules, which distributed energy and time signals to the analog to digital converters (ADCs) and time to digital converters (TDCs). The data acquisition (DAQ) trigger was generated by demanding that at least one arc of any detector fired, achieved by chaining the output of the arc amplifiers. The measurements were made in singles mode, requiring the DAQ to read simultaneously the output of all arcs and sectors that fired, recording events with all multiplicities M. Higher multiplicity requirements were imposed in off-line analysis.

A. Event characterization

Each particle hitting the detector was characterized by its spherical-polar coordinates (θ, ϕ) and its kinetic energy E. The accuracy of the geometrical pixel position calibration was confirmed by comparing the geometrically calculated solid angle of each pixel with that obtained from Rutherford scattering. The scattering angle θ was defined as the angle between the beam axis and the velocity vector of the scattered particle. The azimuthal angle ϕ was defined with $\phi = 0°$ pointing vertically downward. The θ and ϕ coverage was 116.0°–169.0° and 29.5°–328.6°, respectively. The uncertainty in localizing the position of each particle was given by the finite pixel size. To give continuous distributions, the (θ,ϕ) of each particle were randomized within the physical boundaries of its pixel by assuming a uniform distribution of events over the pixel.

Individual energy calibration of each arc and sector of each detector was made using the elastic peaks at all measured energies and the 9.360 MeV decay α line from ^{215}Fr. The nucleus ^{215}Fr is produced following 3n evaporation from the compound nucleus formed in the fusion reaction ^{9}Be + ^{209}Bi

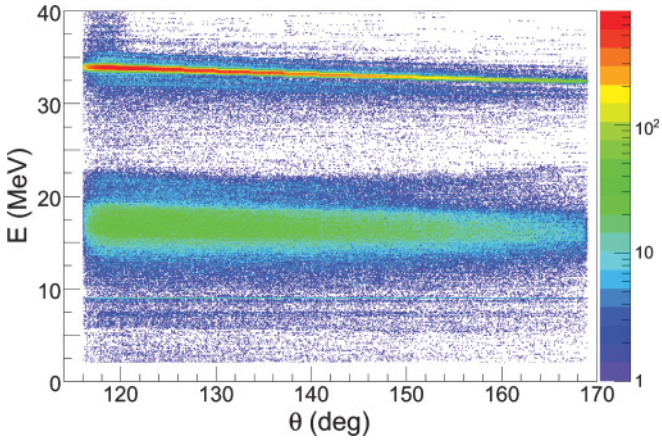

FIG. 2. (Color online) Energy-calibrated singles spectrum for ^{9}Be + ^{209}Bi measured at $E_{\text{c.m.}} = 38.26$ MeV and displayed across the full angular coverage of the array. Events corresponding to elastic scattering (∼34 MeV), breakup of the ^{9}Be (∼17 MeV), and α-decay lines (5–10 MeV) are shown.

at the highest beam energy. Corrections for energy loss in the target were applied event by event in the calibration procedure, and the measurements of breakup fragments, assuming that particles originated from the target midpoint. Energy losses through the Mylar foil in front of each detector and the measured detector dead layer were also included. A typical energy-calibrated singles spectrum for ^{9}Be + ^{209}Bi measured at $E_{\text{c.m.}} = 38.26$ MeV is presented in Fig. 2 and shows elastic events at ∼34 MeV. The α lines between 5 and 10 MeV visible in Fig. 2, with energies independent of angle, originate from the evaporation residues formed following CF and ICF. Between these lines and the elastics lies a broad structure centered at 17 MeV, corresponding to approximately half the energy of the elastically scattered beam particles. An $M = 2$ coincidence requirement selects mainly events in this structure, indicating that these events correspond to two coincident particles likely to be from the breakup of the projectile-like nucleus.

B. Extraction of breakup events

Breakup of ^{9}Be results in two coincident charged fragments, which need to be detected in any two pixels of the array. The pixel that the fragment hits was identified by correlating the energy signal between a (front) arc and a (rear) sector. Identification became complicated only when the coincident pair hit the same arc or sector in a given detector. These events were recovered by matching their energy to the sum of signals measured on the other side of the detector. Sources of spurious coincidences included (i) random coincidences with detector noise or a scattered projectile, (ii) cross-talk across adjacent sectors, and (iii) charge sharing of a scattered projectile that hit the interstrip partition. Contributions to source (i) were removed by applying cuts in the singles energy spectrum to remove the noise and elastic particles. Sources (ii) and (iii) can only originate from coincidences within a single detector, and to remove them events detected in adjacent pixels were rejected. Correlations between the kinetic energies E_1 and E_2 of the coincident fragments over the whole array are

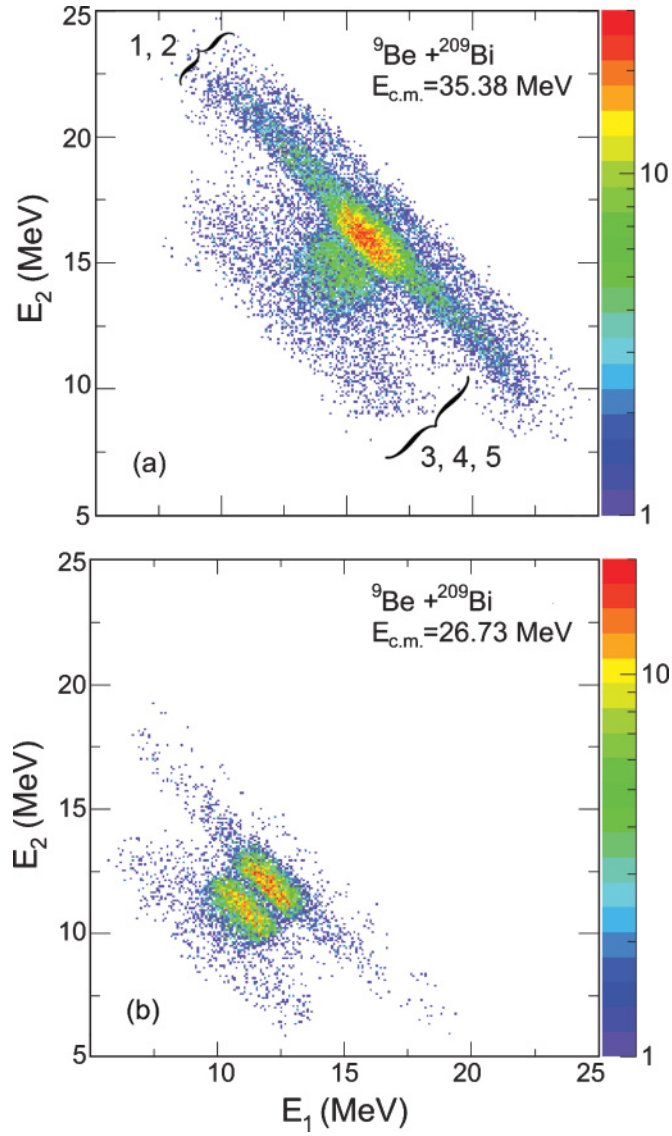

FIG. 3. (Color online) Energy correlation of fragment 1 (E_1) versus fragment 2 (E_2) for ^{9}Be + ^{209}Bi, showing distinct correlations between coincident breakup fragments at two energies as indicated. Regions marked 1–5 (a) are described in Sec. IV.

presented in Fig. 3 for ^{9}Be + ^{209}Bi measured at center-of-mass energies 35.38 MeV [Fig. 3(a)] and 26.73 MeV [Fig. 3(b)]. Assignment of the label 1 or 2 to the particles in a given pair was random. Immediately obvious are the band-like structures, which suggest that the breakup fragments have originated from a number of physical mechanisms. For the majority of events $E_1 \sim E_2$, but certain breakup events display extreme energy ratios between their fragments, and these are present even at deep sub-barrier energies. Further insights into the physical processes that govern breakup were made possible by reconstructing the three-body reaction Q-value.

III. CHARACTERIZING BREAKUP EVENTS

To characterize the α pairs resulting from the breakup of ^{9}Be, the associated reaction Q-value was determined. Because

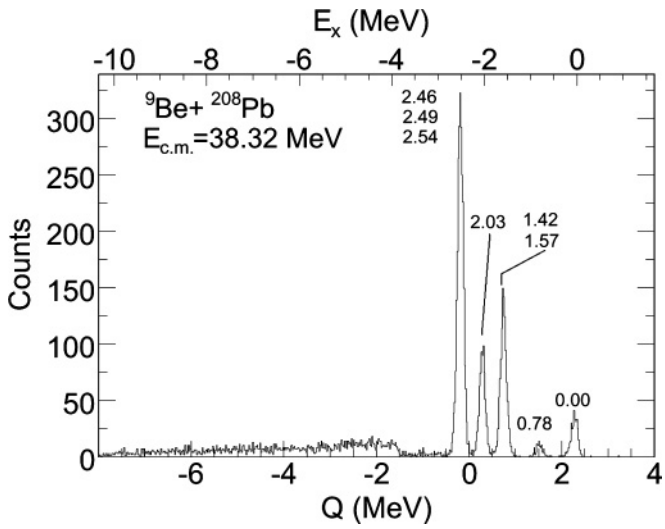

FIG. 4. Reconstructed Q-value spectrum for $^{9}\mathrm{Be} + ^{208}\mathrm{Pb}$ at center-of-mass energy 38.32 MeV. The upper axis gives the excitation energy of ^{209}Pb. Reconstructed Q-values for the peaks match the excitation energies of ^{209}Pb (as labeled), indicating that breakup is triggered by mainly n-transfer.

no information on the fate of the valence neutron was obtained in the measurement, the Q-value reconstruction assumed that the two detected charged particles were the only fragments produced. The three-body Q-value, equal to the difference between initial- and final-state kinetic energies, was obtained by

$$Q = E_1 + E_2 + E_{\mathrm{recoil}} - E_{\mathrm{beam}}, \tag{1}$$

where E_{beam} is the kinetic energy of the beam particle. Knowledge of the undetected recoil energy E_{recoil} was obtained by applying momentum conservation,

$$\vec{p}_{\,\mathrm{beam}} = \vec{p}_{\,1} + \vec{p}_{\,2} + \vec{p}_{\,\mathrm{recoil}}. \tag{2}$$

The reconstructed Q-value spectrum for $^{9}\mathrm{Be} + ^{208}\mathrm{Pb}$, measured at center-of-mass energy 38.32 MeV is presented in Fig. 4. The spectrum shows a series of sharp peaks at $Q > -0.5$ MeV and a rather smooth distribution for $Q < -1.5$ MeV. Sharp peaks imply that the assumed two-body breakup is correct. This can occur through breakup of ^{8}Be following neutron stripping, leaving ^{209}Pb as the residual nucleus. The small number of states at low excitation for ^{209}Pb, compared to other measured targets, allowed for the unambiguous identification of its excited states, the energies of which are labeled in Fig. 4. The peak at the highest value of Q corresponds to $^{209}\mathrm{Pb}^{\mathrm{g.s.}}$, while excited states up to 2.54 MeV have been identified. For the well-defined n-transfer peaks the upper axis corresponds to the excitation energy of ^{209}Pb, identifying the state of the target-like nucleus following breakup. Following n-transfer, the ^{8}Be nucleus may also be produced in any of its excited states. As this excitation energy appears in the kinetic energy of the measured α particles, the reconstructed Q-value is unable to provide any knowledge of the state of the projectile-like nucleus at breakup. However, this information can be obtained from the relative energy E_{12} of the breakup fragments.

Understanding the physical significance of relative energy is best achieved by considering the breakup of an isolated ^{8}Be nucleus. From the kinematics of ^{8}Be ground-state decay (as detailed in Appendix A 1) the two α particles escape in opposite directions, sharing equally the breakup Q-value of 92 keV. If breakup takes place from an excited state of ^{8}Be, then it is the sum of the excitation energy and Q-value that is shared equally between the two α particles. Because the α particles are emitted in opposite directions in the center-of-mass frame, the relative energy of the breakup fragments provides information about the excitation energy of ^{8}Be. In practice the relative energy is calculated from the measured properties of the breakup fragments, utilizing the definition $E_{12} = (m/4)|\vec{v}_{\,1} - \vec{v}_{\,2}|^2$. Here m is the α particle mass and $\vec{v}_{\,1}$ and $\vec{v}_{\,2}$ are the velocity vectors of the breakup fragments. Using the cosine rule, E_{12} can be expressed as

$$E_{12} = \tfrac{1}{2}(E_1 + E_2) - \sqrt{E_1 E_2}\cos\theta_{12}, \tag{3}$$

where the laboratory opening angle between the two α particles θ_{12} is given by

$$\cos\theta_{12} = \cos\theta_1\cos\theta_2 + \sin\theta_1\sin\theta_2\cos(\phi_1 - \phi_2). \tag{4}$$

Figure 5 shows the measured α-α relative energy spectra for $^{9}\mathrm{Be} + ^{209}\mathrm{Bi}$ at all measured energies. The large contribution of $^{8}\mathrm{Be}^{\mathrm{g.s.}}$ decay is clearly seen through its characteristic 92 keV decay energy. The Monte Carlo calculated E_{12} profiles (explained in Appendix A) for $^{8}\mathrm{Be}^{\mathrm{g.s.}}$ decay α pairs are overlain on the measured spectra (shaded peaks). The simulated curves are normalized to the peak of the experimental curves and show excellent agreement with the experimental data. The parent $^{8}\mathrm{Be}^{\mathrm{g.s.}}$ has a width of 5.6 eV [26] and thus a lifetime of 1.2×10^{-16} s, typically traveling a few nanometers before breakup. Thus, $^{8}\mathrm{Be}^{\mathrm{g.s.}}$ formed following the interaction with the target breaks up far from the nuclear interaction region. It therefore is effectively a stable participant in the reaction and its decay or breakup cannot contribute to ICF or to the reduction of CF. Excluding the well-identified contribution of $^{8}\mathrm{Be}^{\mathrm{g.s.}}$, the remainder of the breakup α pairs in Fig. 5 form a broad continuum, without narrow peaks. These events, as identified in the following section, originate from excited states of the projectile-like nucleus with a large width [26] and, thus lifetimes, $\sim 10^{-22}$ s. Here, breakup occurs close to the target nucleus, where interactions of the target with the breakup fragments perturb their velocities and therefore E_{12} is no longer a direct measure of the excitation energy of the projectile-like nucleus. The dominant contribution to this yield is prompt breakup, which is the component that can affect fusion, leading to ICF and hence the suppression of CF [23]. Mechanisms leading to prompt breakup and long-lived $^{8}\mathrm{Be}^{\mathrm{g.s.}}$ have been identified by combining Q-value and E_{12} information as described in Sec. IV.

IV. MECHANISMS TRIGGERING BREAKUP

The physical mechanisms leading to breakup can only be determined with complete knowledge of the origins of all detected α-particle pairs. To achieve this, the two complementary quantities Q-value and E_{12} were utilized, together revealing

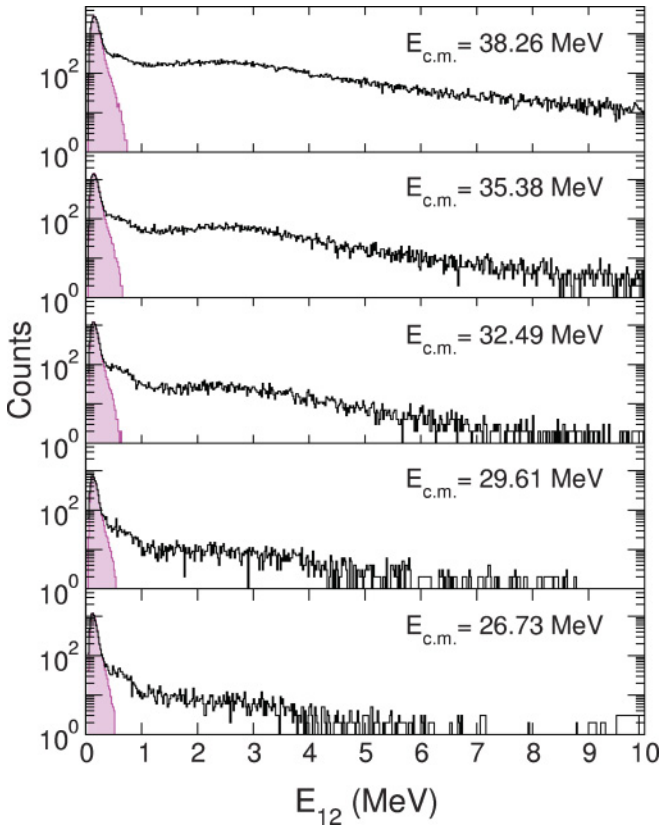

FIG. 5. (Color online) E_{12} distribution for ^{9}Be + ^{209}Bi at all measured energies, as indicated. For each energy the yield is peaked at 92 keV, corresponding to the decay of ^{8}Be$^{g.s.}$. The shaded region shows the calculated E_{12} detector response for ^{8}Be$^{g.s.}$ decay. The upper energy cutoff of 10 MeV is for display only and does not reflect the acceptance of the array.

the complete picture of the dynamics of breakup. Figure 6 shows the Q-value for ^{9}Be + ^{209}Bi measured at center-of-mass energies 35.38 MeV [Fig. 6(a)] and 26.73 MeV [Fig. 6(b)] plotted against the relative energy. The vertical dashed line separates, in relative energy, the α pairs resulting from the decay of ^{8}Be$^{g.s.}$ from those originating from the breakup of excited states of the projectile-like nucleus. The solid horizontal line separates events that can only originate from the breakup of the projectile-like nucleus following n-stripping (above the line) and events resulting from breakup following the excitation of the projectile [29] as well as possible transfer (below the line). The yield from the region below the solid line will be identified as 'inelastic,' even though it can include a very small component from transfer. The two lines divide the two-dimensional spectrum into four distinct regions, labeled 1, 2, 3, and 5. Region 4 is considered a special subset of region 5, details of which follow. Table II is a complete summary of the mechanisms that (ultimately) result in the breakup of the projectile-like nucleus.

A. n-transfer forming ^{8}Be

The α pairs in regions 1 and 2 originate from a ^{8}Be parent nucleus that is produced following n-transfer from the ^{9}Be projectile to the target. **Region 1** [^{209}Bi(^{9}Be,^{8}Be$^{g.s.}$)^{210}Bi] corresponds to ^{8}Be formed in its ground state, with ^{210}Bi populated mainly in excited states, as evidenced by the spread in Q-values. Events corresponding to the weak population of the ^{210}Bi$^{g.s.}$ are at a Q-value of 2.94 MeV. **Region 2** [^{209}Bi(^{9}Be,^{8}Be*)^{210}Bi] identified by the parallel Q-value bands at E_{12} higher than those for ^{8}Be$^{g.s.}$, correspond to the breakup of ^{8}Be from excited states with large width, leading to prompt breakup, and hence a large relative energy between the α pair. These large E_{12} events seem likely to arise from breakup via the 3.04 MeV (2^{+}) and 11.35 MeV (4^{+}) excited states of ^{8}Be, which have a width of 1.5 MeV and 3.5 MeV, respectively [26]. The strongly populated transfer states of region 2 are to the same excited states in ^{210}Bi as in region 1.

B. Projectile excitation

Below the solid line in Fig. 6, at negative Q-values, lie breakup events that mainly originate from the excitation of the projectile to energies above its cluster breakup threshold [^{209}Bi(^{9}Be,^{9}Be*)^{209}Bi]. The strongly populated **region 3** corresponds to ^{8}Be$^{g.s.}$ decay [^{9}Be* $\rightarrow$ ^{8}Be$^{g.s.}$ + n]. The sum of regions 1 and 3 includes all α pairs that originate following the decay of the ^{8}Be$^{g.s.}$ parent nucleus and do not contribute to prompt breakup.

Projecting the events below the solid horizontal line onto the E_{12} axis, a clear peak is present at $E_{12} \sim 0.6$ MeV. This peak has been previously attributed to breakup from the 2.429 MeV $5/2^{-}$ state in ^{9}Be [30–32]. The peak, seen as a distinct clustering of events with low E_{12} and Q (between -8 and -3 MeV) in Fig. 6, is labeled **region 4**. The concentration of these events at small E_{12} values is because of the long lifetime of this state (8.4×10^{-19} s [26]), which means that breakup occurs long after its interaction with the target and outside the nuclear interaction region on its outgoing trajectory. Owing to the long lifetime, events in this region do not contribute to the prompt breakup yield and have been excluded. It has been reported in

TABLE II. Summary of mechanisms triggering the breakup of ^{9}Be. See text for details.

Region	Time scale	Primary reaction	Breakup mode	Particles produced
1	10^{-16} s	^{A}X(^{9}Be,^{8}Be$^{g.s.}$)$^{A+1}$X	^{8}Be$^{g.s.}$ $\rightarrow \alpha + \alpha$	α, α
2	Prompt	^{A}X(^{9}Be,^{8}Be*)$^{A+1}$X	^{8}Be* $\rightarrow \alpha + \alpha$	α, α
3	10^{-16} s	^{A}X(^{9}Be,^{9}Be*)^{A}X	^{9}Be* $\rightarrow$ ^{8}Be$^{g.s.}$ + n	α, α, n
4	10^{-18} s	^{A}X(^{9}Be,^{9}Be$^{5/2^-}$)^{A}X	^{9}Be$^{5/2^-}$ $\rightarrow$ ^{8}Be^{2+} + n	α, α, n
			^{9}Be$^{5/2^-}$ $\rightarrow$ ^{5}He$^{g.s.}$ + α	α, α, n
5	Prompt	^{A}X(^{9}Be,^{9}Be*)^{A}X	Unknown	α, α, n

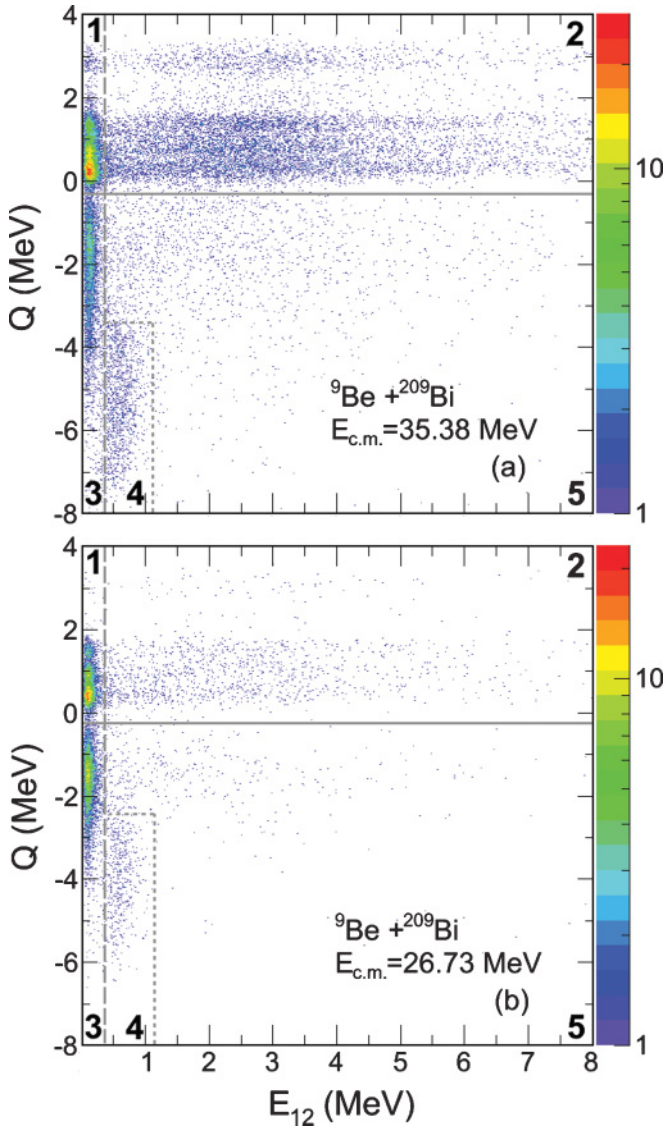

FIG. 6. (Color online) Two-dimensional spectra of Q-value against E_{12} plotted for ^{9}Be + ^{209}Bi at two energies as indicated. The reaction Q-value and E_{12} together reveal the complete picture of the dynamics of breakup. See text for details.

Refs. [32–34] that decay from the 2.429 MeV excited state in ^{9}Be occurs primarily via the ^{8}Be$^{2+} + n$ channel, while contributions from the ^{5}He$^{g.s.} + \alpha$ channel have not been excluded. Both these decay modes result in the emission of a neutron, which is not measured in this experiment. In the absence of information on the energy of the neutron, the Q-value cannot be determined event by event.

Region 5 consists of prompt breakup events with large E_{12}, originating following the excitation of ^{9}Be. Similarly to region 4, the neutron information is lost and therefore the Q-values cannot be determined. The sum of regions 2 and 5 constitutes the prompt breakup events. It is evident from Fig. 6 that the inelastic contribution to prompt breakup (region 5) is much less significant than that from n-transfer (region 2).

C. Correlation between E_1 vs E_2 and Q vs E_{12}

With the physical origins of the features characterized in Fig. 6, it is interesting to correlate these with the primary observables E_1 and E_2 in Fig. 3. The two modes of α-pair production can be clearly distinguished. The band with high $E_1 + E_2$ results from n-transfer (regions 1 and 2 in Fig. 6) and is well separated from projectile excitation (regions 3, 4, and 5 in Fig. 6). The yield from ^{8}Be$^{g.s.}$ decay dominates each band (clearly seen for $E_{c.m.} = 26.73$ MeV at $E_1 \sim E_2$) and has a narrow energy distribution. The α-α coincidences originating from the decay of excited states of ^{8}Be produced following neutron transfer (region 2 in Fig. 6) form a broad energy distribution as background to the narrow n-transfer-originated ^{8}Be$^{g.s.}$ band (region 1 in Fig. 6). The broad energy distribution of the inelastic events corresponding to direct projectile breakup (regions 4 and 5 in Fig. 6) is background to the narrow ^{8}Be$^{g.s.}$ energy band formed following projectile excitation (region 3 in Fig. 6).

D. Q vs E_{12} for other targets

Figure 7 displays the reconstructed Q-value vs E_{12} spectra for reactions of ^{9}Be with ^{208}Pb, ^{196}Pt, ^{186}W, and ^{144}Sm targets for the center-of-mass energies indicated. The Q-value for ground-state n-transfer is marked by a dashed line. The general features highlighted in Fig. 6 are present for all the targets. The group of events attributed to breakup via the long-lived 2.429 MeV excited state in ^{9}Be (region 4 in Fig. 6) is present for all targets (circled). While the ^{9}Be + ^{209}Bi and ^{9}Be + ^{208}Pb reactions appear to allow a separation between breakup following n-transfer and that following inelastic excitation of ^{9}Be, this separation is not possible for the other targets owing to the overlap in Q-values between these processes. However, all measurements show a clear separation among ^{8}Be$^{g.s.}$ decay, breakup from ^{9}Be$^{5/2^-}$, and prompt breakup.

V. BREAKUP YIELDS

As described in the previous section, the Q vs E_{12} spectra allow a clear separation between prompt breakup and the decay of long-lived states of the projectile-like nucleus and between transfer and inelastic contributions for the ^{208}Pb and ^{209}Bi targets. To quantify individual contributions, their integrated yields need to be normalized and efficiency corrected. The quantity of interest is the breakup probability $P_{\rm BU}$ given by

$$P_{\rm BU} = \frac{N_{\rm BU}^{\rm bin}}{\epsilon} \frac{1}{N_{\rm Ruth}^{\rm bin}}, \tag{5}$$

where $N_{\rm BU}^{\rm bin}$ is the breakup counts and $N_{\rm Ruth}^{\rm bin}$ is the number of elastic counts that would have been observed in the case of pure Rutherford scattering, for a given θ bin. The efficiency of detecting both breakup α particles, where in the absence of breakup the parent nucleus would have been detected in the θ bin, is given by ϵ. Its calculation was made separately for ^{8}Be$^{g.s.}$ and prompt breakup. The calculated efficiency was found to be nearly independent of the beam energy for both prompt breakup and ^{8}Be$^{g.s.}$ decay. The efficiency correction technique is detailed in Appendix B. The elastic counts

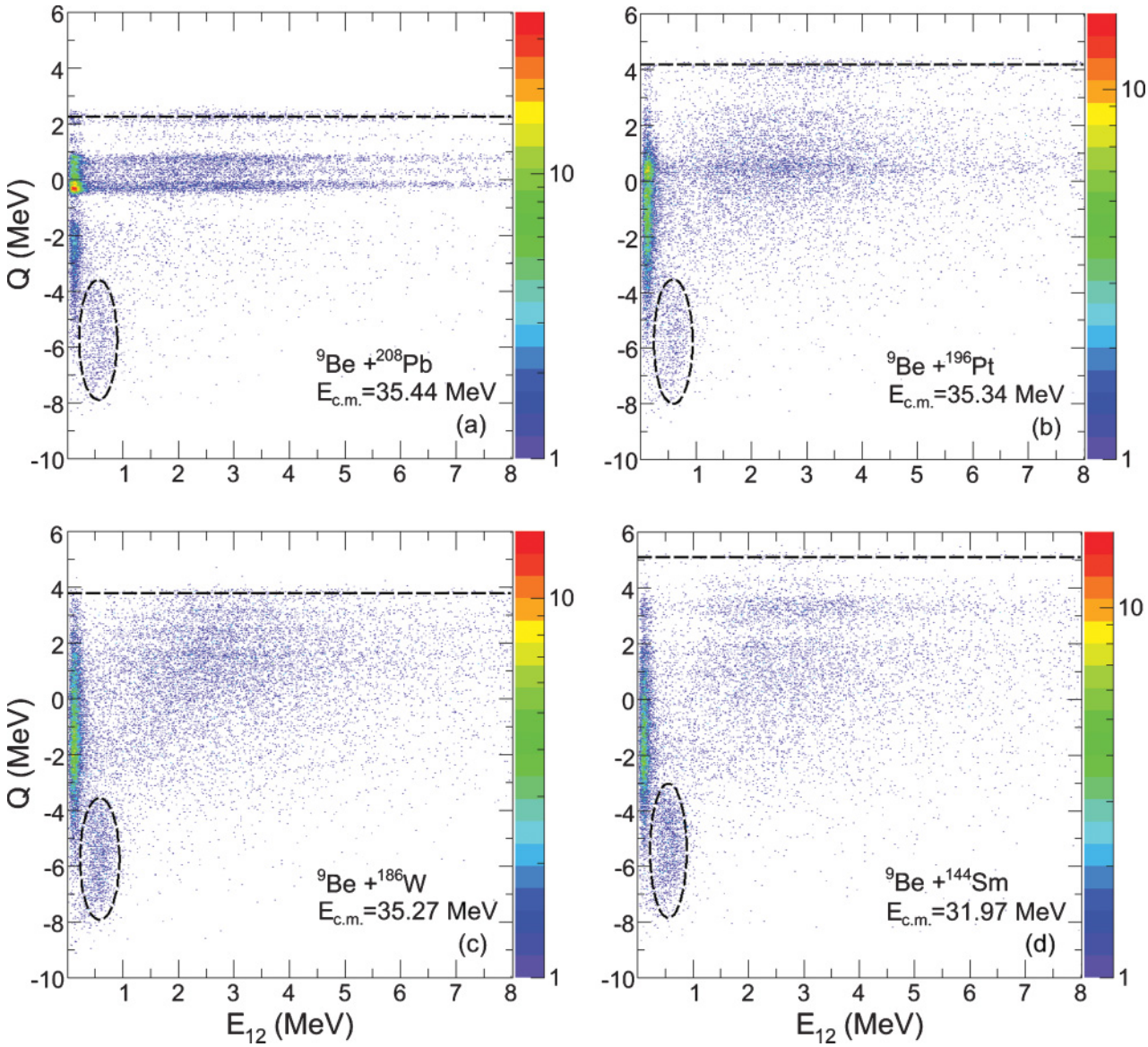

FIG. 7. (Color online) Reconstructed Q-value plotted against the relative energy of the two α particles for the reactions and energies indicated. The dashed line is drawn at the Q-value for n-transfer to the recoil ground state. Events originating from the long-lived 2.429 MeV state in ^{9}Be are circled.

$N_{\rm el}^{\rm norm}$ within the 124°–127° θ bin, which are pure Rutherford for all targets at deep sub-barrier energies, were used for normalization. The Rutherford counts in the normalizing θ bin $N_{\rm Ruth}^{\rm norm}$ are related to $N_{\rm Ruth}^{\rm bin}$ by

$$N_{\rm Ruth}^{\rm bin} = N_{\rm Ruth}^{\rm norm} \frac{\left(\frac{d\sigma_{\rm Ruth}}{d\Omega}\right)_{\rm bin}}{\left(\frac{d\sigma_{\rm Ruth}}{d\Omega}\right)_{\rm norm}} \left(\frac{d\Omega^{\rm bin}}{d\Omega^{\rm norm}}\right), \tag{6}$$

where $(d\sigma_{\rm Ruth}/d\Omega)_{\rm x}$ and $d\Omega^{\rm x}$ are the differential cross sections and solid angles, respectively. For near-barrier energies, where elastic scattering at 124°–127° can deviate from Rutherford scattering, corrections were applied using the ratio of the differential elastic cross sections to that of Rutherford scattering, $d\sigma_{\rm el}/d\sigma_{\rm Ruth}$, measured for ^{9}Be + ^{208}Pb [35]:

$$N_{\rm Ruth}^{\rm norm} = \frac{N_{\rm el}^{\rm norm}}{\left(\frac{d\sigma_{\rm el}}{d\sigma_{\rm Ruth}}\right)_{\rm norm}}. \tag{7}$$

The same correction was applied to all targets at equal values of the ratio of the center-of-mass energy to the fusion barrier energy $E_{\rm c.m.}/V_b$. The fusion barrier energies (listed in Table I) were calculated using the Sao Paulo potential (SPP) [27,28]. The SPP calculation is able to reproduce, within uncertainties, the experimentally determined barriers of 38.3 ± 0.6 and 31.2 ± 0.3 MeV for ^{9}Be + ^{208}Pb [4] and ^{9}Be + ^{144}Sm [17], respectively, proving the reliability of the calculation. The $P_{\rm BU}$ could then be calculated by combining Eqs. (5)–(7).

Before reporting the final $P_{\rm BU}$ values, the consistency of the raw detector counts, without detector efficiency correction,

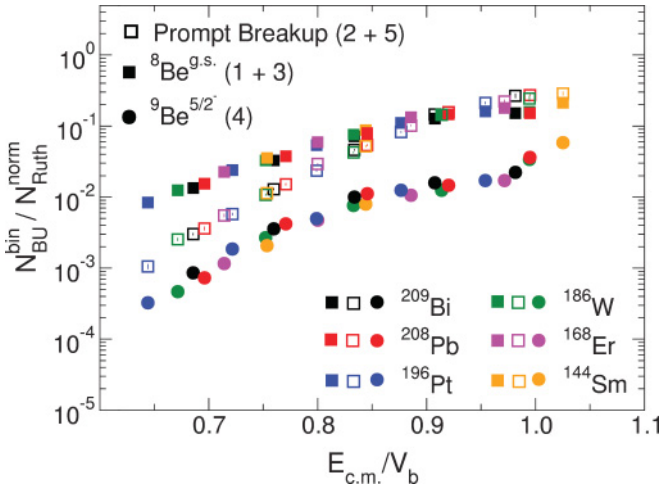

FIG. 8. (Color online) Ratio of the raw breakup counts across the entire array to the corrected Rutherford normalizing counts, as a function of the ratio of the center-of-mass energy to the SPP [27,28] calculated barrier energy. The yields for prompt breakup and decay from ^{8}Be$^{g.s.}$ and ^{9}Be$^{5/2^-}$ long-lived states are displayed individually. Numbers in parentheses correspond to regions 1–5 in Fig. 6.

is presented. The ratio of the breakup counts, measured across the entire array, to the corrected Rutherford counts [Eq. (7)] in the 124°–127° bin $N_{BU}^{bin}/N_{Ruth}^{norm}$ are plotted as a function of $E_{c.m.}/V_b$ in Fig. 8. Contributions from prompt breakup and decay from long-lived states (^{8}Be$^{g.s.}$ and ^{9}Be$^{5/2^-}$) are presented separately. Although the breakup counts are not efficiency corrected, all modes of breakup behave similarly as a function of energy. At sub-barrier energies ($E_{c.m.}/V_b < 0.95$), all components show an exponential rise with increasing energy. However, at near-barrier energies, where the probability of fragment capture by the target is no longer negligible, and consequently flux is removed from NCBU, all yields fall below the exponential trend. The calculation of the prompt breakup probability functions, as detailed in Sec. VI, have made use of the exponential region ($E_{c.m.}/V_b < 0.95$) only.

VI. BREAKUP SYSTEMATICS

For describing the systematics of breakup, a suitable quantity is the breakup probability as a function of the distance of closest approach $R_{min}(\theta_{c.m.})$ of the two interacting nuclei for a Coulomb trajectory. The usefulness of the breakup probability function was highlighted in Ref. [23], where the relationship among CF, ICF, and sub-barrier NCBU was first introduced through the breakup function. The three-dimensional classical dynamical reaction model [24], which was subsequently developed, characterized the classical orbit of the projectile in terms of the distance of closest approach.

A. $R_{min}(\theta_{c.m.})$ determination

The distance of closest approach on a classical Coulomb trajectory is related to the scattering angle $\theta_{c.m.}$ by

$$R_{min} = \frac{Z_P Z_T e^2}{2E_{c.m.}}\left(1 + \frac{1}{\sin\left(\frac{\theta_{c.m.}}{2}\right)}\right), \qquad (8)$$

where Z_P and Z_T are the charge of the projectile and target, respectively. In determining the R_{min} dependence of the breakup probability, the detector array was divided into three equal-width θ bins, assigning the scattering angle at the center of each bin to $\theta_{c.m.}$.

Each θ bin was chosen to cover a laboratory angular range of 15°, whose boundaries were 121°|136°|151°|166°. The laboratory angle for each breakup event was defined as the scattering angle of the parent ^{8}Be $\theta_{^8Be}$ under the assumption of a ^{8}Be parent nucleus for each coincident α pair (i.e., $\vec{p}_{^8Be} = \vec{p}_1 + \vec{p}_2$). The dominance of breakup triggered by n-transfer, producing ^{8}Be (Fig. 6), justifies this assumption. $\theta_{^8Be}$ is determined from conservation of momentum,

$$p_{^8Be}\cos\theta_{^8Be} = p_1\cos\theta_1 + p_2\cos\theta_2, \qquad (9)$$

which, for events originating from ^{8}Be$^{g.s.}$, lies at approximately $\frac{1}{2}(\theta_1 + \theta_2)$. Consequently for each θ bin the calculated probability of breakup was assigned an R_{min} value calculated using its center-of-mass central scattering angle.

B. The breakup probability function

The breakup probabilities as a function of R_{min} for ^{9}Be + ^{208}Pb are presented in Fig. 9 for decay of ^{8}Be$^{g.s.}$ [Fig. 9(a)] and for prompt breakup [Fig. 9(b)]. Both modes of breakup have been further divided into their transfer (squares) and inelastic (circles) components. Also shown are the measurements from Ref. [23] (open symbols), obtained from the sum of the α-doubles yield for ^{8}Be$^{g.s.}$ decay and from the α-singles spectrum for total prompt breakup. The probabilities for total prompt breakup (triangles) are in excellent agreement with the measurements from Ref. [23], validating the current, more complex experimental technique.

Deviations from the exponential nature of the breakup probability in Fig. 9(a) are most obvious for the smallest R_{min} values (corresponding to $E_{c.m.}/V_b > 0.95$ in Fig. 8), as absorption by the target depletes the breakup yield. Figure 9(b) demonstrates the dominance of prompt breakup following neutron transfer from ^{9}Be to the target nucleus. The transfer component is nearly one order of magnitude greater than that for breakup following projectile excitation. The dominance of n-transfer could be related to the weak binding of the valence neutron in ^{9}Be. Large 1n- and 2n-transfer cross sections have also been measured for ^{6}He, where the two-neutron separation energy is <1 MeV [36,37].

C. Prompt breakup as a function of R_{min} and surface separation

Figure 10(a) shows the measured prompt breakup probabilities for all reactions studied. The data are presented only for energies below the Coulomb barrier, where the fragment capture cross section by the target nucleus is negligible ($E_{c.m.}/V_b < 0.95$ in Fig. 8). The prompt breakup probabilities show exponential variation with R_{min}. Given that the breakup probability is transfer dominated, one may expect that the surface separation rather than R_{min} should be the critical variable controlling breakup. Surface separation has been defined as the difference between the distance of closest approach and the summed radii of the interacting

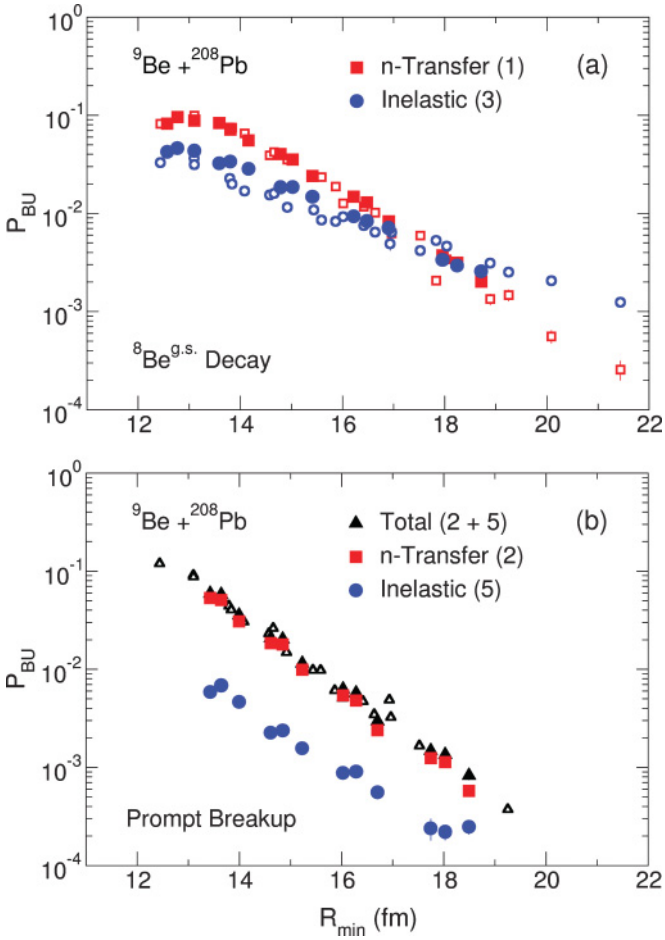

FIG. 9. (Color online) Breakup probability for n-transfer-initiated breakup (squares) and breakup following projectile excitation (circles) for the ^{9}Be + ^{208}Pb reaction. Data are divided into decay of ^{8}Be$^{g.s.}$ (a) and prompt breakup (b). Open symbols are from Ref. [23], measured for ^{9}Be + ^{nat}Pb. Numbers in parentheses correspond to regions 1–5 in Fig. 6.

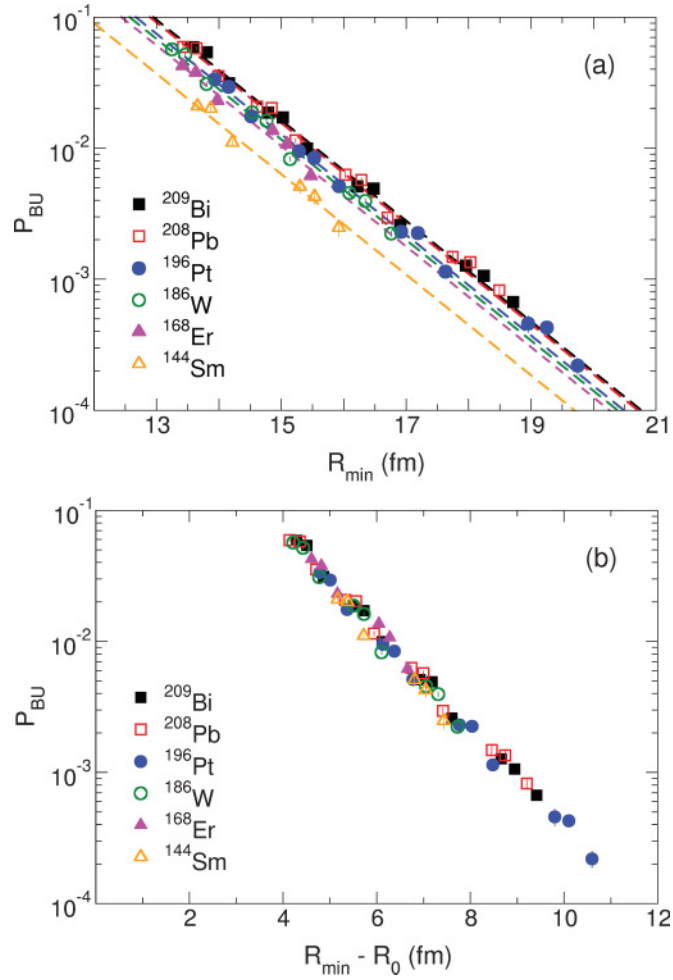

FIG. 10. (Color online) Plot of the measured prompt breakup probability (a) and the probability of breakup as a function of target-projectile surface separation $R_{min} - R_0$ (b) for all reactions studied. Data points displayed are for sub-barrier and deep sub-barrier energies, where the breakup yield is nearly unaffected by capture of the projectile or its charged fragments by the target. Dashed lines represent least-squares exponential fits for each measured reaction (for details see Sec. VII A). Eliminating the effect of nuclear size, the breakup process shows no significant dependence on the target nucleus but varies strongly with the surface separation.

nuclei $R_0 = R_P + R_T$, where R_P and R_T are the radii of the equivalent spherical nuclei, calculated using a radius parameter of 1.2 fm. The breakup probability is presented in Fig. 10(b) as a function of $R_{min} - R_0$. The effect of nuclear size is removed, and strikingly the breakup probabilities for all targets ranging in atomic number between 62 and 83 overlap. Thus the breakup process only varies strongly with the surface separation and shows no significant dependence on the target nucleus structure, despite the dominance of neutron transfer as the trigger for breakup.

VII. MAPPING SUB-BARRIER BREAKUP TO ABOVE-BARRIER COMPLETE FUSION SUPPRESSION

Having determined experimentally the radial dependence of the sub-barrier breakup probabilities, it is possible to predict above-barrier yields for CF and ICF using the code PLATYPUS [24]. This code is based on a three-body classical trajectory model with stochastic breakup. It relates the no-capture sub-barrier breakup measurements to above-barrier CF and ICF cross sections. The initial two-body problem consists of a target and a weakly bound clustered projectile that follows a Rutherford orbit. Breakup is defined through an empirically obtained local breakup probability function P^{L}_{BU}(R), where R is the projectile-target (P-T) radial separation. The experimentally measured breakup probability function P_{BU} [Fig. 10(a)] is the integral of $P^{L}_{BU}(R)$ along the classical orbit of the projectile,

$$P_{BU}(R_{min}) = 2\int_{R_{min}}^{\infty} P^{L}_{BU}(R)dR. \quad (10)$$

The factor of 2 results from the fact that breakup may occur on the incoming or outgoing branch of the trajectory. Its exponential nature, as shown in Fig. 10, will place maximum

TABLE III. The radius parameter r_0 (fm) used in PLATYPUS calculations for ^{8}Be and α on target T. Values have been adjusted to reproduce the s-wave SPP [27,28] barrier energies.

	^{209}Bi	^{208}Pb	^{196}Pt	^{186}W	^{168}Er	^{144}Sm
^{8}Be + T	1.432	1.432	1.434	1.435	1.438	1.444
α + T	1.481	1.481	1.484	1.489	1.494	1.504

likelihood of breakup at $R_{\min}$. At breakup, conditions such as the projectile excitation energy, fragment separation, and orientation of α particles are Monte Carlo sampled [24]. In determining the location where breakup takes place, the breakup function was Monte Carlo sampled out to 50 fm. As the model is limited to solving a three-body problem, the calculations were made for a ^{8}Be projectile, modeled as an α-α cluster. The present measurements, which show that prompt ^{9}Be breakup occurs dominantly through an excited ^{8}Be nucleus, validate the approximation of a ^{9}Be projectile by ^{8}Be.

The parametrization of the Coulomb and nuclear potential was the same as that used in Ref. [24]. The pre- and post-breakup Coulomb interactions between the participants (i.e., P-T, α_1-T, α_2-T, and α_1-α_2) were taken as those between a point charge and a spherical charge distribution of charge radius $R_C = 1.2A_T^{1/3}$ fm. The nuclear potential was parameterized by a Woods-Saxon potential, $V(r) = -V_0(1 + e^{(r-r_0A_T^{1/3})/a_0})^{-1}$. Following Ref. [24] the values of the depth V_0 and diffuseness a_0 were set to 120.9 MeV and 0.76 fm for P-T and 62.0 MeV and 0.62 fm for the α-T interaction, respectively. The radius parameter r_0 was adjusted such that the s-wave SPP-calculated barrier energy [27,28] was reproduced for each reaction. The r_0 values used for P-T and α-T are reported in Table III. The α_1-α_2 parameters utilized were as defined in Ref. [24].

A. PLATYPUS breakup function

The empirical input for PLATYPUS was obtained by making a least-squares fit to the data with the functional form of P_{BU} given by

$$P_{BU}(R_{\min}) = e^{(\nu+\mu R_{\min})} \tag{11}$$

for each of the measured reactions. The parametrization of the breakup function makes use of the parameters μ and ν, representing the logarithmic slope and intercept of the function, respectively. The measured slopes for the reactions are presented in Fig. 11, and their corresponding values are listed in Table IV. Within their estimated uncertainties the values are independent of Z_T, with a mean value of $\overline{\mu} = -(0.884 \pm 0.011)$ fm^{-1}, represented by the dashed line in Fig. 11. The mean slope was utilized to obtain an intercept parameter for each target, values of which are presented in Table IV. The dashed lines in Fig. 10(a) represent the least-squares fits to the experimental points made using $\overline{\mu}$ and the individual intercept parameters given in Table IV.

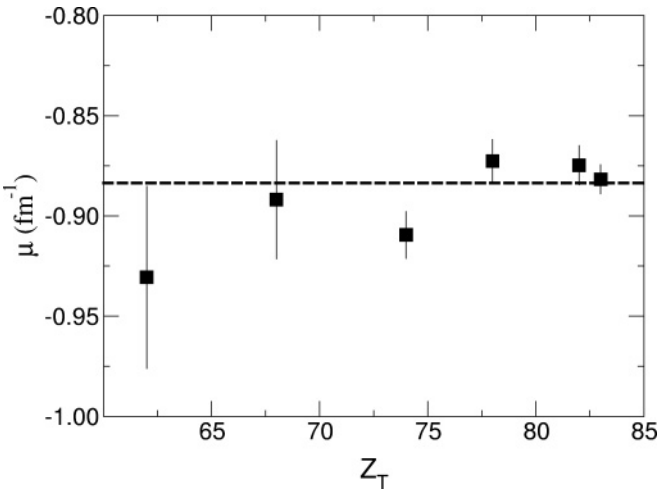

FIG. 11. Slope parameters μ (fm^{-1}) obtained from the measured $P_{\rm BU}(R_{\min})$ for prompt breakup. The dashed line represents the weighted mean value of μ.

B. Systematics of incomplete fusion

The breakup function for each target was used as input to PLATYPUS to obtain the CF and ICF cross sections at above-barrier energies. In the model, CF occurs if the ^{8}Be projectile penetrates the radius of the ^{8}Be + T s-wave Coulomb barrier or the time evolution of the α_1 and α_2 breakup fragments take both of them inside the α-T barrier radius. ICF occurs when a single α particle penetrates the radius of the α-T s-wave Coulomb barrier. Both cross sections are calculated using a sharp cutoff in angular momentum. In the calculations a sample of 1200 incident projectiles per partial wave was used, and waves up to 120$\hbar$ were included to ensure the convergence of the cross sections.

The cross sections calculated by PLATYPUS were utilized to investigate the systematics of CF suppression owing to breakup. In making comparisons between the various reactions, the probability of ICF (F_{ICF}), defined as the ratio of ICF to total fusion (ICF + CF), was calculated for above-barrier energies in the range 1.05–1.28V_b. Figure 12 shows the calculated CF suppression factors for all measured reactions as a function of the charge of the target nucleus, allowing comparisons to be made.

The open circles mark the suppression factor obtained using the mean slope of $\overline{\mu} = -(0.884 \pm 0.011)$ fm^{-1} and the associated intercepts from Table IV. These show a slight increase with increasing projectile charge, indicating a very

TABLE IV. Slope parameter μ and uncertainty σ_μ obtained by making an exponential least-squares fit to the measured breakup function. Intercept parameter ν and uncertainty σ_ν were obtained by fitting the measured breakup function using the mean slope.

	^{209}Bi	^{208}Pb	^{196}Pt	^{186}W	^{168}Er	^{144}Sm
μ (fm^{-1})	−0.882	−0.875	−0.873	−0.909	−0.891	−0.930
σ_μ (fm^{-1})	0.007	0.010	0.011	0.012	0.030	0.045
ν	9.138	9.089	8.890	8.801	8.686	8.191
σ_ν	0.009	0.012	0.012	0.011	0.014	0.020

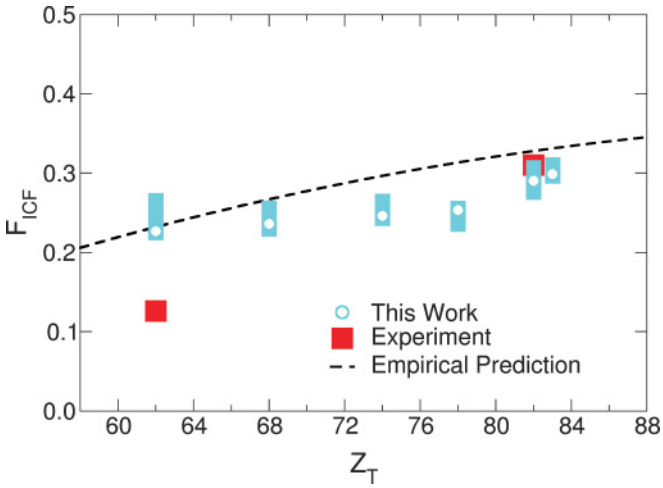

FIG. 12. (Color online) The net effect of breakup on fusion presented as the ICF probability as a function of the target atomic number. The filled rectangles represent the sensitivity of the model-predicted CF suppression factors to uncertainties in the slope parameter of the breakup function. The open circles correspond to calculations made using the common slope and intercept values in Table IV. The experimental values [12,17] are presented by the solid squares for ^{9}Be + ^{144}Sm and ^{9}Be + ^{208}Pb. The dashed line is the empirical prediction of Ref. [23].

slight rise in suppression of fusion with an increase in target atomic number. The rectangles around the circles represent the limits of the prediction based on the individual experimental uncertainties in the slopes of the breakup functions for each target. To obtain the limits, the $\mu + \sigma_\mu$ and $\mu - \sigma_\mu$ values for the slope were fixed and two new intercepts, ν_1 and ν_2, were obtained by making a least-squares fit to Fig. 10(a). Following this, the CF and ICF cross-section calculations were made with the PLATYPUS breakup function parameterized with $(\mu + \sigma_\mu, \nu_1)$ and $(\mu - \sigma_\mu, \nu_2)$.

Within the limits defined based on the experimental uncertainty in μ, it may be concluded that the CF suppression is nearly independent of Z_T, and therefore $Z_P Z_T$, for the measured range of atomic numbers in this work. This behavior of ^{9}Be is consistent with the direct measurement of above-barrier ICF of ^{6,7}Li and ^{10}B, incident on a range of heavy targets, for which the systematics extracted in Ref. [21] showed their CF suppression factor to be independent of $Z_P Z_T$ within their experimental uncertainties.

The dashed line represents the empirical CF suppression factor prediction made in Ref. [23]. The prediction assumes that the breakup probability depends on the gradient of the nuclear potential, exponentially on the surface separation, and independent of nuclear structure. Also shown in Fig. 12 are the ^{9}Be + ^{208}Pb and ^{9}Be + ^{144}Sm F_{ICF} obtained from direct ICF and CF cross-section measurements. To allow comparisons to be made with the PLATYPUS ICF and CF cross sections, the experimental F_{ICF} was determined from above-barrier measurements of ICF and CF cross sections [12,17] and its value for each target is equal to the weighted average F_{ICF} in the energy range 1.05–1.28V_b. The model-predicted F_{ICF} for ^{9}Be + ^{208}Pb is in agreement with its experimental value. Although the model-predicted F_{ICF} for ^{9}Be + ^{144}Sm displays agreement with the empirical prediction, it overestimates the experimentally determined ratio for ^{9}Be + ^{144}Sm. This discrepancy may be attributable to the fact that the measured ICF cross section was a lower limit only, as it did not include contributions from ^{146}Gd and ^{148}Gd [17].

VIII. CONCLUSIONS

A large-solid-angle Si detector array has been used to make sub-barrier breakup measurements for the weakly bound ^{9}Be projectile incident on ^{209}Bi, ^{208}Pb, ^{196}Pt, ^{186}W, ^{168}Er, and ^{144}Sm. Here capture of the charged fragments by the target is negligible. The angle and energy resolution provided by the 512-pixel array allowed determination of the reaction Q-value and the relative energy of the two coincident breakup α particles. These two quantities, in combination, permitted complete characterization of the state of both the target-like and the projectile-like nucleus following their interaction.

The prompt breakup yield could be separated from the 10^{-16} s lifetime ground-state decay of ^{8}Be and from the 10^{-18} s decay of the 2.429 MeV excited state of ^{9}Be. These long-lived states have characteristic narrow relative energy distributions, signaling that breakup occurs on the projectile outgoing trajectory and far away from the nuclear interaction region. Compared to the fusion time scale, they are essentially stable participants in the reaction and cannot contribute to ICF.

The wide relative energy distributions for the prompt breakup events arise as breakup of the projectile-like nucleus occurs close to the target. The origin of the prompt breakup was investigated in detail for the ^{9}Be + ^{208}Pb reaction. It was possible to make a further separation of the prompt breakup into its components arising from inelastic and n-stripping reactions. The probability of prompt breakup following n-transfer was found to be 10 times larger than following inelastic interaction.

The prompt breakup probability for all targets was parameterized in terms of the distance of closest approach on a Coulomb trajectory. The probability of breakup was found to have an exponential dependence on the surface-to-surface separation of the interacting nuclei but appears to be essentially independent of the target nucleus. The measured sub-barrier breakup probabilities were related to the above-barrier CF and ICF cross sections using a three-body classical dynamical model [24]. The results show that complete fusion suppression at above-barrier energies is almost independent of the target atomic number for the range of measured targets.

The conclusion that breakup is mainly triggered by n-stripping is an important ingredient for breakup models. Because n-transfer is also the dominant reaction mechanism for the breakup of n-rich beams, quantal models developed to describe breakup of ^{9}Be will be of relevance to understanding the fusion and breakup of n-rich unstable nuclei.

ACKNOWLEDGMENTS

The authors would like to acknowledge A. Muirhead and T. Kitchen for their exceptional technical contributions in preparing for this experiment. This work was supported by an ARC Discovery Grant.

APPENDIX A: MONTE CARLO SIMULATION OF ^{8}Be$^{g.s.}$ DECAY

The relative energy E_{12} of ^{8}Be$^{g.s.}$ decay is 92 keV. However, the energy resolution and pixelation of the array will spread the reconstructed E_{12} around this value. The shape of the experimental E_{12} spectrum was calculated using a Monte Carlo simulation. The simulation program consisted of two modules, which handled (1) the physical description of asymptotic breakup and (2) incorporation of the pixelation and energy resolution of the detector array. Module (1) calculates the kinematics of the reaction in the laboratory frame, determining the kinetic energy and spatial coordinates of the breakup fragments. Module (2) includes the spatial (angular) and energy resolution of the array.

1. Kinematics of asymptotic breakup

^{8}Be is produced in its ground state following a primary two-body reaction A(a, b)B, where projectile a is incident on target A, forming ejectile b and recoil B. The laboratory (labeled LAB) and center-of-mass (labeled C.M.) frames for this two-body reaction are presented in Fig. 13. The ^{8}Be$^{g.s.}$ subsequently decays into α particles c and d, which are emitted back to back in the center-of-mass frame of the ^{8}Be, and with $J^\pi = 0^+$, their distribution is isotropic. Their velocity vectors define a center-of-mass breakup sphere that is represented by the dashed circle in Fig. 13. The breakup process is independent of the mechanism that resulted in the production of ^{8}Be in its ground state, from which it inherits only its Q-value. The 1.2×10^{-16} s lifetime of ^{8}Be$^{g.s.}$ means that it typically travels a few nanometers before breakup. Hence its breakup occurs at its asymptotic velocity, far outside the nuclear interaction region, and is referred to as asymptotic breakup.

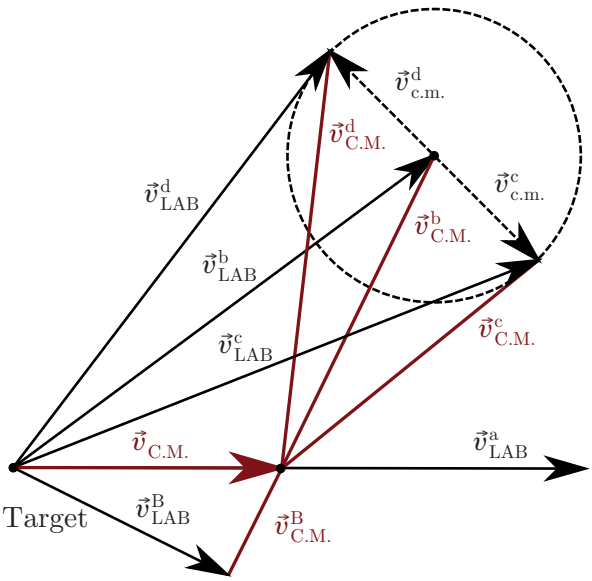

FIG. 13. (Color online) Velocity diagram displaying the laboratory and center-of-mass frames for decay of ^{8}Be$^{g.s.}$. The dotted circle represents the center-of-mass breakup sphere for ^{8}Be$^{g.s.}$. See text for details.

The target nucleus with mass m_A is at rest in the laboratory frame and the ^{9}Be projectile with mass m_a is incident with velocity $\vec{v}^{\,a}_{LAB}$. The velocity of the center of mass is given by

$$\vec{v}_{C.M.} = \frac{m_a}{m_a + m_A}\vec{v}^{\,a}_{LAB}. \tag{A1}$$

The magnitude of the ^{8}Be center-of-mass velocity $\vec{v}^{\,b}_{C.M.}$ is given by

$$v^b_{C.M.} = \sqrt{\frac{2}{m_b}\left\{\frac{(E_a + Q)(m_A m_B)}{(m_a + m_A)(m_b + m_B)}\left[1 + \frac{m_a Q}{m_A(E_a + Q)}\right]\right\}}, \tag{A2}$$

where m_b and m_B are the masses of the ejectile and recoil, respectively, and E_a is the laboratory energy of projectile a. Using energy and momentum conservation the ejectile laboratory velocity can be expressed as

$$\vec{v}^{\,b}_{LAB} = \vec{v}^{\,b}_{C.M.} + \vec{v}_{C.M.}. \tag{A3}$$

Asymptotic breakup occurs in the center-of-mass frame of the ejectile and with an isotropic α-particle distribution. The magnitude of the velocity of each fragment is given by

$$v^{c,d}_{c.m.} = \sqrt{\frac{Q}{m_{c,d}}}, \tag{A4}$$

where $Q = 92$ keV is the ^{8}Be$^{g.s.}$ decay energy. Subsequently the laboratory velocity and energy of each breakup fragment are obtained from

$$\vec{v}^{\,c,d}_{LAB} = \vec{v}^{\,b}_{LAB} + \vec{v}^{\,c,d}_{c.m.}. \tag{A5}$$

2. Incorporation of array spatial and energy resolution

Corrections for the spatial resolution of the array, owing to the finite pixel size, were made to simulated breakup fragments incident on the detector array by randomizing the spatial coordinates of each reconstructed fragment within the physical boundaries of its pixel. The broadening of the simulated events in Fig. 5 is primarily because of the spatial resolution of the array, which is dominant in determining the resolution of E_{12}. The $\sigma = 50$ keV measured energy resolution of the detectors was incorporated into the reconstructed kinetic energy of the breakup fragments by adding a normally distributed random deviation characterized by $\sigma = 50$ keV.

APPENDIX B: DETECTOR ARRAY EFFICIENCY

Calculation of efficiency for the detection of coincident α particles, following the decay of ^{8}Be$^{g.s.}$ and prompt breakup,

is described. The former uses the Monte Carlo calculation for asymptotic breakup (Appendix A). The code PLATYPUS, based on a classical trajectory model for breakup [24], was used for the latter.

1. ^{8}Be$^{g.s.}$ efficiency calculation

The efficiency ϵ for capture of α pairs originating from ^{8}Be$^{g.s.}$ is given by

$$\epsilon^{^8\mathrm{Be}^{g.s.}}_{\theta_n-\theta_m} = \frac{N_{BU}^{\phi_1\leqslant\phi\leqslant\phi_2}}{N_{BU}^{0\leqslant\phi\leqslant 2\pi}}, \tag{B1}$$

where N_{BU} is the number of breakup events in each θ bin with azimuthal limits ϕ_1 and ϕ_2. The azimuthal limits on the numerator define the geometrical coverage of the array and the detected breakup events were filtered by the effect of rejection of coincident events in adjacent pixels, as in the analysis of the experimental data. The calculation was made for each θ bin defined by the limits of θ_n and θ_m. The array was divided into three 15° θ bins with the limits of 121°|136°|151°|166°. The efficiency correction was applied individually to the transfer and inelastic components by utilizing the corresponding weighted Q-value average in calculating the breakup kinematics. Typical efficiency values are 15% at forward angles, increasing to 40% for backward angles, where the reduced pixel size reduces the effect of rejection of α particles incident on adjacent pixels on the ^{8}Be$^{g.s.}$ efficiency (see Sec. II B).

2. Prompt efficiency calculation

The correlation of α pairs calculated by PLATYPUS was utilized to obtain the efficiency for detection of prompt breakup events at energies below the barrier. The classical model means that there is no quantum tunneling and hence no capture at below-barrier energies, so that the contribution from NCBU becomes unity.

To calculate the efficiency, a sample of $N^{\ell}_{BU} = 100$ ^{8}Be projectiles was generated for partial wave $\ell = 0$, and weighted geometrically by $2\ell + 1$ for higher ℓ values. The breakup probability for each partial wave P^{ℓ}_{BU} was calculated using the breakup function. Partial waves up to $\ell_{max} = 100$ have been included, at which the probability of breakup P^{ℓ}_{BU} reaches 10^{-8} that of the s wave. The prompt efficiency within each 15° θ bin is given by

$$\epsilon^{\mathrm{prompt}}_{\theta_n-\theta_m} = \frac{\left[\sum_{\ell=0}^{100} N^{\ell}_{BU} P^{\ell}_{BU}\right]^{\phi_1\leqslant\phi\leqslant\phi_2}}{\left[\sum_{\ell=0}^{100} N^{\ell}_{BU} P^{\ell}_{BU}\right]^{0\leqslant\phi\leqslant 2\pi}}. \tag{B2}$$

The azimuthal limits on the numerator define the geometrical coverage of the array and the detected breakup events were filtered by the effect of rejection of coincident events in adjacent pixels, as in the analysis of the experimental data. The prompt efficiency values were nearly independent of beam energy and typically varied between 25% (corresponding to $121^\circ \leqslant \theta \leqslant 136^\circ$) and 42% (corresponding to $136^\circ \leqslant \theta \leqslant 151^\circ$) across the detector array.

[1] L. F. Canto *et al.*, Phys. Rep. **424**, 1 (2006), and references therein.
[2] J. F. Liang and C. Signorini, Int. J. Mod. Phys. E **14**, 1121 (2005), and references therein.
[3] N. Keeley *et al.*, Prog. Part. Nucl. Phys. **59**, 579 (2007), and references therein.
[4] M. Dasgupta *et al.*, Phys. Rev. Lett. **82**, 1395 (1999).
[5] C. Signorini *et al.*, Eur. Phys. J. A **5**, 7 (1999).
[6] S. B. Moraes *et al.*, Phys. Rev. C **61**, 064608 (2000).
[7] M. Dasgupta *et al.*, Phys. Rev. C **66**, 041602(R) (2002).
[8] V. Tripathi, A. Navin, K. Mahata, K. Ramachandran, A. Chatterjee, and S. Kailas, Phys. Rev. Lett. **88**, 172701 (2002).
[9] I. Padron *et al.*, Phys. Rev. C **66**, 044608 (2002).
[10] C. Beck *et al.*, Phys. Rev. C **67**, 054602 (2003).
[11] Y. W. Wu *et al.*, Phys. Rev. C **68**, 044605 (2003).
[12] M. Dasgupta *et al.*, Phys. Rev. C **70**, 024606 (2004).
[13] G. V. Marti *et al.*, Phys. Rev. C **71**, 027602 (2005).
[14] P. R. S. Gomes *et al.*, Phys. Rev. C **71**, 034608 (2005).
[15] A. Shrivastava *et al.*, Phys. Lett. **B633**, 463 (2006).
[16] L. R. Gasques, M. Dasgupta, D. J. Hinde, T. Peatey, A. Diaz-Torres, and J. O. Newton, Phys. Rev. C **74**, 064615 (2006).
[17] P. R. S. Gomes *et al.*, Phys. Rev. C **73**, 064606 (2006).
[18] A. Mukherjee *et al.*, Phys. Lett. **B636**, 91 (2006).
[19] P. K. Rath *et al.*, Phys. Rev. C **79**, 051601(R) (2009).
[20] P. R. S. Gomes, J. Lubian, and L. F. Canto, Phys. Rev. C **79**, 027606 (2009).
[21] L. R. Gasques, D. J. Hinde, M. Dasgupta, A. Mukherjee, and R. G. Thomas, Phys. Rev. C **79**, 034605 (2009).
[22] M. Dasgupta *et al.*, Annu. Rev. Nucl. Part. Sci. **48**, 401 (1998), and references therein.
[23] D. J. Hinde, M. Dasgupta, B. R. Fulton, C. R. Morton, R. J. Wooliscroft, A. C. Berriman, and K. Hagino, Phys. Rev. Lett. **89**, 272701 (2002).
[24] A. Diaz-Torres, D. J. Hinde, J. A. Tostevin, M. Dasgupta, and L. R. Gasques, Phys. Rev. Lett. **98**, 152701 (2007).
[25] A. Diaz-Torres *et al.*, Phys. Lett. **B533**, 265 (2002).
[26] D. R. Tilley *et al.*, Nucl. Phys. **A745**, 155 (2004), and references therein.
[27] L. C. Chamon *et al.*, Phys. Rev. C **66**, 014610 (2002).
[28] M. A. G. Alvarez *et al.*, Nucl. Phys. **A723**, 93 (2003).
[29] D. P. Stahel, G. J. Wozniak, M. S. Zisman, B. D. Jeltema, and J. Cerny, Phys. Rev. C **16**, 1456 (1977).
[30] J. Mösner *et al.*, Nucl. Phys. **64**, 169 (1965).
[31] B. R. Fulton *et al.*, Phys. Rev. C **70**, 047602 (2004).
[32] N. I. Ashwood *et al.*, Phys. Rev. C **72**, 024314 (2005).
[33] P. Papka *et al.*, Phys. Rev. C **75**, 045803 (2007).
[34] T. A. D. Brown *et al.*, Phys. Rev. C **76**, 054605 (2007).
[35] R. J. Woolliscroft, B. R. Fulton, R. L. Cowin, M. Dasgupta, D. J. Hinde, C. R. Morton, and A. C. Berriman, Phys. Rev. C **69**, 044612 (2004).
[36] J. P. Bychowski *et al.*, Phys. Lett. **B596**, 26 (2004).
[37] P. A. DeYoung *et al.*, Phys. Rev. C **71**, 051601(R) (2005).